

## Supplementary Materials for

### **Energy Autonomous Paper Modules and Functional Circuits**

Jing Han,<sup>‡a,b</sup> Nuo Xu,<sup>‡a,c</sup> Jinran Yu,<sup>a,b</sup> Yifei Wang,<sup>a,b</sup> Yao Xiong,<sup>a,b</sup> Yichen Wei,<sup>a,c</sup> Zhong Lin Wang,<sup>\*a,b,d</sup> Qijun Sun<sup>\*a,b,c</sup>

<sup>a</sup>Beijing Institute of Nanoenergy and Nanosystems, Chinese Academy of Sciences, Beijing, 101400, China

<sup>b</sup>School of Nanoscience and Technology, University of Chinese Academy of Sciences, Beijing, 100049, China

<sup>c</sup>Center on Nanoenergy Research, School of Physical Science and Technology, Guangxi University, Nanning, 530004, China

<sup>d</sup>School of Materials Science and Engineering, Georgia Institute of Technology, Atlanta, Georgia 30332-0245, United States

<sup>‡</sup>These authors contributed equally to this work.

<sup>\*</sup>To whom the correspondence should be addressed.

Email: [sunqijun@binn.cas.cn](mailto:sunqijun@binn.cas.cn); [zhong.wang@mse.gatech.edu](mailto:zhong.wang@mse.gatech.edu)

Keywords: energy autonomous, paper module, self-powered systems, power management, functional circuits

## Supplementary Note

1. *Explanation of the variation tendency of open-circuit voltage ( $V_{OC}$ ), short-circuit current ( $I_{SC}$ ), and transferred charges ( $Q_{SC}$ ) for the paper-TENG module:* The variation tendency of  $V_{OC}$ ,  $I_{SC}$ , and  $Q_{SC}$  can be explained by the following explanations. According to the Gauss theorem, the voltage between the two electrodes can be given by

$$V = -\frac{Q}{S\epsilon_0}\left(\frac{d}{\epsilon} + x(t)\right) + \frac{\sigma x(t)}{\epsilon_0} \quad (1)$$

where  $Q$  is the amount of transferred charge between the fluorinated ethylene propylene (FEP) friction layer and the CNT/Au electrode and  $x$  is the separation distance between the two friction layers.  $d$ ,  $S$ , and  $\epsilon$  are the thickness, electrode area and relative dielectric constant of the FEP, respectively.  $\epsilon_0$  is the permittivity of vacuum.

Equation (1) is the basic equation for the contact-separation mode TENG and can be utilized to calculate its output property. Commonly, there are two special cases to be analyzed: the open-circuit (OC) condition and short-circuit (SC) conditions. Under OC conditions, there is no charge transfer, which means that  $Q$  is 0. Therefore, the open-circuit voltage  $V_{OC}$  is given by:

$$V_{OC} = \frac{\sigma x(t)}{\epsilon_0} \quad (2)$$

We can see that the  $V_{OC}$  as a function of both  $x(t)$  and the static charge density of  $\sigma$  is mainly determined by the structures and the selected materials of the TENG, which shows no response to frequency.

By comparison, the  $I_{SC}$  varies with the varied frequency:

$$I_{sc} = \frac{dQ_{SC}}{dt} = \frac{S\sigma d + \sigma(t)dx}{(d + x(t))^2 dt} = \frac{S\sigma dv(t)}{(d + x(t))^2} \quad (3)$$

where  $v(t)$  is a function of time and is determined by the contact-separation rate of the FEP film and CNT/Au electrode. This equation means that the  $I_{SC}$  is proportional to the static charge density of  $\sigma$  and the contact-separation rate of  $v(t)$ . Therefore, an increased contact-separation frequency can increase the current output of the paper-TENG module.

The TENG is referred to as capacitive conduction, in which the current is the only conduction mechanism for electricity transport. The surface charge density  $\sigma$  increases with the number of contact-separation between the two friction materials and eventually reaches saturation. Keithley 6514 measures the total transfer charge of a TENG, so the transfer charge  $Q_{SC}$  does not change with frequency and is represented as a constant.

2. *Characterization of energy transfer efficiency  $\eta_E$  for the power management circuit (PMC) module:* The energy transfer efficiency  $\eta_E$ , which is defined as the ratio of the energy stored in  $C_1$  ( $E_{C_1}$ ) to the total energy transferred out from  $C_0$  ( $E_{C_0}$ ), can be given by:

$$\eta_E = \frac{E_{C_1}}{E_{C_0}} \times 100\% \quad (4)$$

The energy transfer efficiency evaluates the energy transfer efficiency from the small capacitor  $C_0$  to the large capacitor  $C_1$ . The  $C_0$  utilized in this experiment is a 1  $\mu\text{F}$  capacitor and the  $C_1$  utilized in this experiment is a 1.1 mF capacitor. Two voltmeters (Keithley 6514) are used to measure  $V_{C_0}$  and  $V_{C_1}$  simultaneously. After extracting the initial and final values of  $V_{C_0}$  ( $V_{2,i}$  and  $V_{1,i}$ ), the energy stored in  $C_0$  and  $C_1$  can be calculated as:

$$E_{C_0} = \frac{1}{2} C_0 \sum_i^{42} (V_{2,i}^2 - V_{1,i}^2) \quad (5)$$

The capacitor  $C_0$  is charged and discharged 42 times in 600 s. The highest value ( $V_{2,i}$ ) and lowest value ( $V_{1,i}$ ) of the voltage are extracted to calculate the energy generated by  $C_0$ , which is evaluated to be 276  $\mu\text{J}$  according to equation (5).

Within 600 s, the initial value ( $V_2$ ) and final value ( $V_1$ ) of  $C_1$  are 0.24 and 0.71 V, respectively. The energy of capacitor  $C_1$  is calculated to be 245.57  $\mu\text{J}$  based on the following equation:

$$E_{C_1} = \frac{1}{2} C_1 (V_2^2 - V_1^2) \quad (6)$$

3. *Characterization of power management efficiency  $\eta_P$  for the PMC module:* The power management efficiency  $\eta_P$ , which is defined as the ratio of the power stored in  $C_2$  ( $P_{C_2, \max}$ ) to the maximum instantaneous power generated from the paper-based triboelectric nanogenerator (paper-TENG,  $P_{TENG, \max}$ ), is expressed by:

$$\eta_P = \frac{P_{C_2, \max}}{P_{TENG, \max}} \times 100\% \quad (7)$$

The paper-TENG is driven by the mechanical motion of palm tapping to evaluate  $P_{TENG, \max}$ . A voltmeter is connected to the parallel resistors ( $R$  at different resistances) to monitor the voltage drop, and the corresponding current signals can be calculated by Ohm's law (**Figure S10a**). According to equation (7), the maximum instantaneous power of the TENG is calculated to be 179.6  $\mu\text{W}$  (**Figure 4d**).

The energy consumed by capacitor  $C_2$  can be evaluated according to the resistance connected in parallel with  $C_2$ .

$$P_{C_2} = \frac{V_{C_2}^2}{R} \quad (8)$$

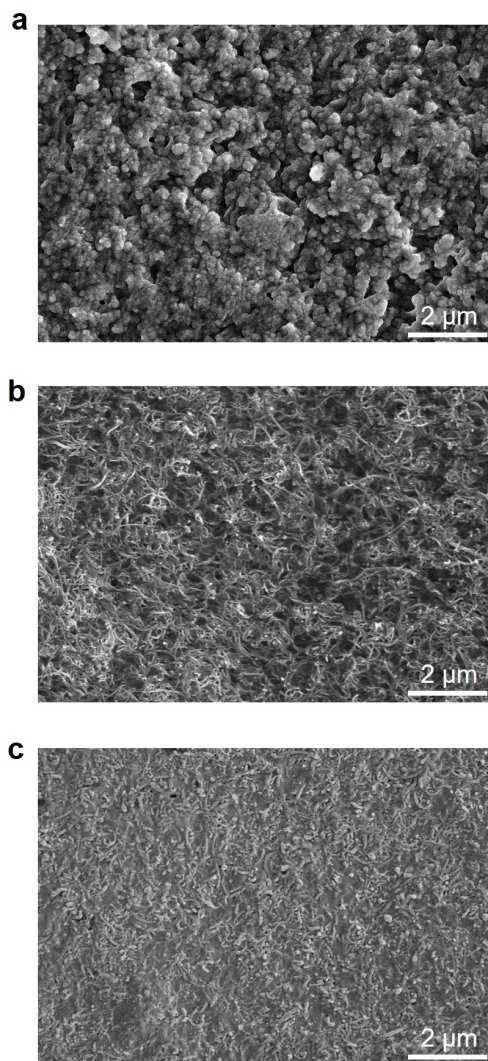
When  $R$  is small (10 and 43 k $\Omega$ ), the power consumed by the resistance is large, and the power produced by the TENG cannot be supplied to the capacitor  $C_2$ . Therefore, the voltage of  $C_2$  decreases with time, and a negative slope of the  $V_{C_2}$ - $t$  curve (**Figure 4c**) can be observed from the voltmeter in parallel with  $C_2$  (Keithley 6514). When  $R$  increases (100 and 1000 k $\Omega$ ), the power consumed by  $R$  gradually decreases and more power is supplied to  $C_2$  from palm tapping. When the slope of the  $V_{C_2}$ - $t$  curve ( $R = 65$  k $\Omega$ ) is 0, the power consumed by  $R$  is equal to the power stored in  $C_2$ . In this case, the energy consumed by capacitor  $C_2$  is calculated to be 96.2  $\mu$ W by equation (8). Accordingly, the power management efficiency is calculated to be 96.2  $\mu$ W/179.6  $\mu$ W = 53.6%.

## Supplementary Figures

### 1. Material characterization of the Teslin paper, CNTs, and CNT/Au electrodes

Teslin paper combines the strength and dimensional stability of polyolefin with the absorbency of silica to form a unique microporous matrix (**Figure S1a**). It has excellent durability benefits not available from competing synthetic paper stocks, including abrasion/scuff-resistance, water-resistance, chemical-resistance, thermal stability, tear-resistance and conformability, sterilization compatibility, ink and toner protection, and lamination/finish friendliness. To prepare good conductors on the unique microporous surface of Teslin paper and ensure excellent conductivity of the electrodes (or interconnections) for the mounted electronic elements, CNTs solution are first coated on the Teslin paper by a bar-coating process to flatten the surface (CNTs are interlocked with each other and exhibit typical morphology with branched-structures, **Figure S1b**). Then Au electrodes are deposited on the CNT film to fill the branched structures and further flatten the surface (**Figure S1c**).

Regarding the performance priority in the sustainable paper modules, the hybrid CNT/Au conducting layer is used as the versatile electrodes for all the paper modules, including the contact-electrification electrodes, current collectors for supercapacitors, and interconnections for basic electronic elements. The hybrid CNT/Au conducting layer is compatible with the facile laser engraving technique, which can be readily patterned in the desired layout in one-step and used for different modules on demand.



**Supplementary Figure 1 | Materials characterization for the Teslin paper, CNTs and CNTs/Au electrodes.** Scanning electron microscope (SEM) images of **a**, Teslin paper, **b**, Teslin paper with coated CNTs, and **c**, Teslin paper with CNTs/Au hybrid electrodes.

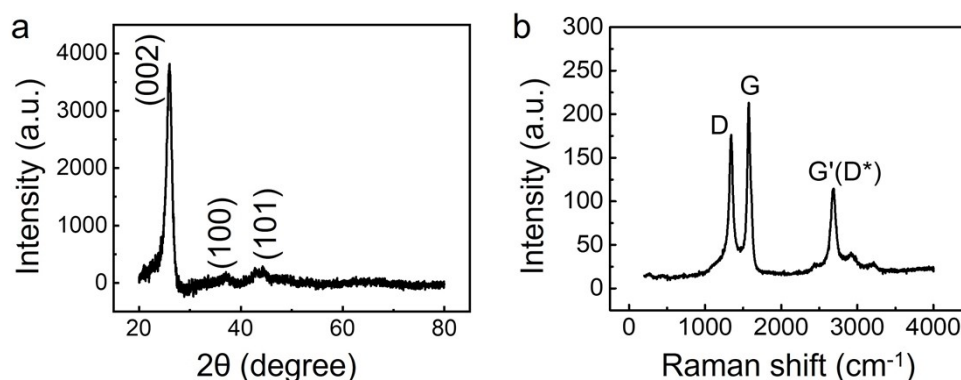
## 2. X-ray diffraction (XRD) and Raman spectroscopy of CNTs

According to the theoretical structural model, CNTs can be regarded as a sleeve structure made of graphite curled along a certain vector direction, so the carbon atomic lamellae is perpendicular to the carbon nanotube axial direction, which means that the preferred orientation of carbon nanotubes is (002) crystalline plane. From the XRD spectrum (**Figure S2a**), it can be observed that the diffraction peak of (002) crystal plane is sharper near  $2\theta = 26^\circ$ , which consists with the characteristic peak of CNTs. There are two broad and weak peaks at  $37.1^\circ$  and  $44.3^\circ$ . These peaks correspond to the (100) and (101) crystallographic planes of carbon, which are the standard diffraction peaks for carbon materials.

The regular molecular structure of CNT determines its characteristics to exhibit Raman scattering phenomena under laser excitation. As CNT can be regarded as a seamless cylinder

rolled up from graphene, it contains all the Raman scattering properties of graphite. Meanwhile, the unique structure of CNT delivers some unique Raman properties (**Figure S2b**), including the defective vibrational mode characteristic peak (D peak,  $1324.66\text{ cm}^{-1}$ ), the tangential stretching mode characteristic peak band (G peak,  $1574.14\text{ cm}^{-1}$ ), and the G' peak (also known as the D\* peak, which is a multiple of the D peak,  $2689.23\text{ cm}^{-1}$ ).

The D mode and D\*(G') mode are both second-order Raman signals, and their peak positions are strongly dependent on the excitation light energy. In carbon materials, the Raman peak between  $1250\text{-}1450\text{ cm}^{-1}$  is usually called D-mode, which comes from lattice defects, and it is generally believed that in-plane substitution defects, vacancies, grain boundaries, and size effects can lead to D-mode generation. In order to reduce the tendency to deviate from the hexagonal stacking of graphite and to reduce the increase in energy of the system, it is possible to adjust the nanotube structure and eliminate the stress between graphite layers by defects, thus CNTs are commonly defective. The D\*(G') mode is the multiplicative peak of the D mode, which is one of the main Raman peaks of CNTs and frequently occurs at  $2500\text{-}2900\text{ cm}^{-1}$ . While the G mode of CNTs comes from the vibration of carbon atoms within the surface of CNTs, i.e., the tangential vibration of carbon atoms, and frequently occurs at  $1500\text{-}1600\text{ cm}^{-1}$ . The relative intensities of the D and G peaks ( $I_D/I_G$ ) reflect the degree of disorder and the density of defects in the sample, which is calculated to be  $I_D/I_G = 0.83$  and indicates a high degree of ordering of the CNTs.

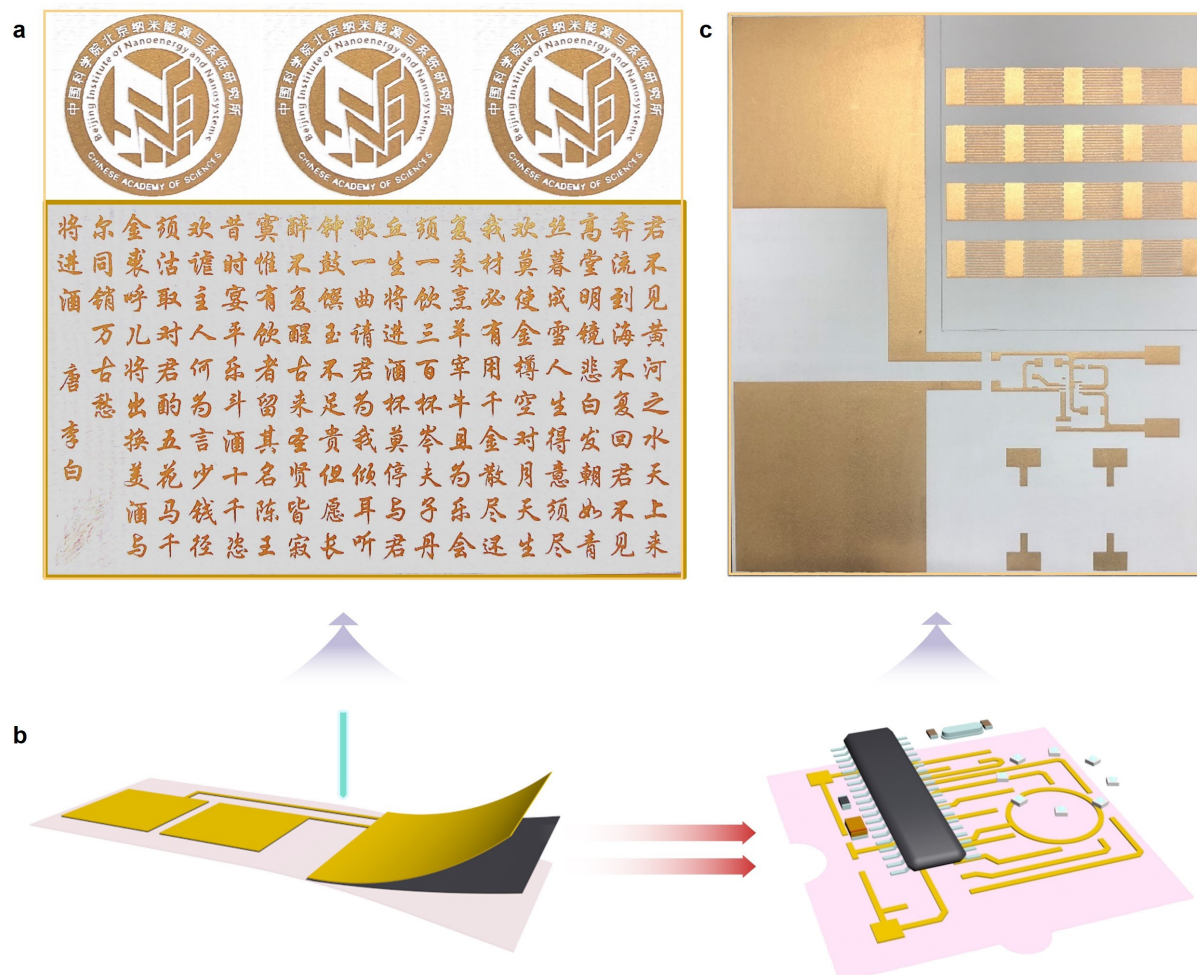


**Supplementary Figure 2 | XRD and Raman spectroscopy of CNTs. a,** XRD spectrum of CNTs. **b,** Raman spectrum of CNTs.

### 3. Laser engraving process for patterning CNTs/Au electrodes, current collectors, interconnections, and desired patterns.

The laser engraving process is utilized to pattern the electrodes and interconnections as it is time-efficient, scalable, customizable, free from photomasks/printing-medium, and high throughput (**Figure S3a**). The basic electronic elements (e.g., rectifier bridge, capacitor,

inductor, microcontroller, etc.) can be precisely assembled and sintered at desired interconnections after laser-engraving (**Figure S3b**). The circuit layouts for TENG, PMC, and MSC modules can be patterned on one piece of large-size paper in one step and prepared for usage after tailoring (**Figure S3c**).

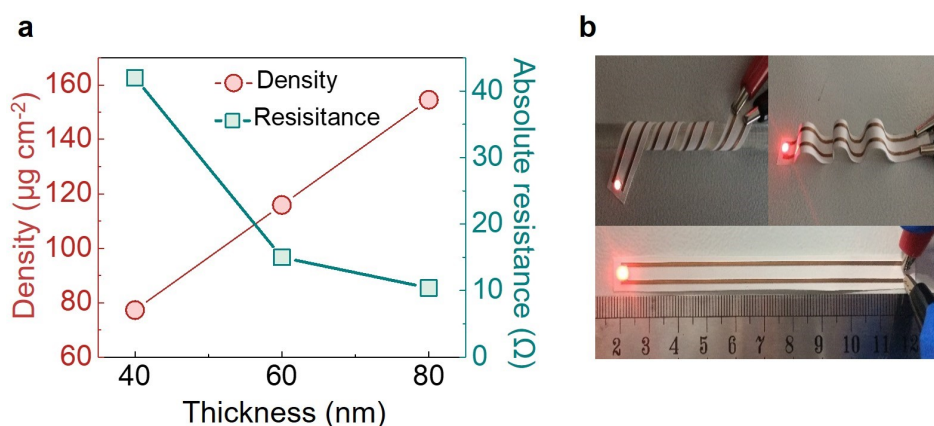


**Supplementary Figure 3 | Laser engraving process for patterning CNTs/Au electrodes, current collectors, interconnections, and desired patterns.** **a**, Laser-engraving process patterned traditional Chinese ancient poem of “Qiang Jin Jiu” by Li Bai and logo of “BINN”. **b**, Schematic illustration of the fabrication process by laser engraving. **c**, Photo images of the laser-engraving processed electrodes/interconnects for TENG, PMC, and MSC in one step.

#### 4. Characterization of CNT/Au electrodes with different Au thicknesses and larger lengths

Although the resistance of CNT electrodes drops by two orders of magnitude with increasing width, it is still too high to be directly used as an interconnection for electronic elements. Nonetheless, the porous and branch-structured morphology of CNTs promises to have a high specific surface area, which is beneficial for rapid ion transport and is capable of working as a

current collector for the MSCs in energy storage modules. Depositing metallic materials on CNT films can effectively decrease the resistance of the as-prepared hybrid electrodes. As shown in **Figure 1g**, its resistance (5 mm width hybrid electrode) can be dramatically decreased from 784 to 21.3  $\Omega$  when 40 nm Au is deposited on the CNT film (CNTs/Au-40). When the Au films are deposited to be 60 or 80 nm, the resistance can be further decreased to below 10  $\Omega$  (CNTs/Au-60 is 6  $\Omega$ , CNTs/Au-80 is 4.6  $\Omega$ ). As the specific density of CNTs/Au-60 paper is also smaller than that of the CNTs/Au-80 paper electrode (**Figure S4a**), we reasonably select CNTs/Au-60 as the standard electrodes for the functional paper modules in the following tests. **Figure S4b** further shows the available lighting of LEDs based on circumvolute or wavy paper electrodes with a large length of 10 cm and width of 2 mm.

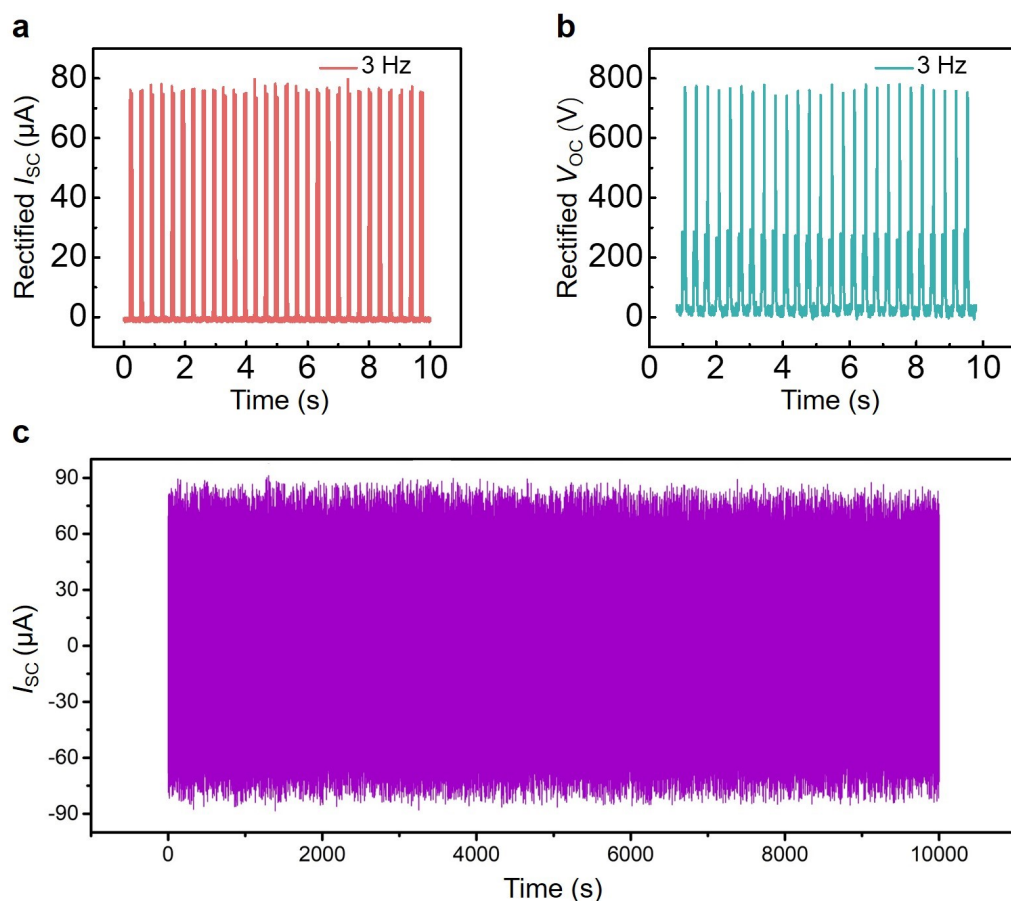


**Supplementary Figure 4 | Characterization of CNTs/Au electrodes with different Au thicknesses and larger lengths.** **a**, Absolute resistances and densities of CNTs/Au hybrid electrodes vs. Au layer thickness. **b**, Lighting of LED based on circumvolute or wavy paper electrodes with a larger length of 10 cm.

## 5. Rectified electrical outputs and durability of the paper-TENG module

The rectified  $I_{sc}$  and  $V_{OC}$  electrical output stability of the TENG is shown in **Figure S5a** and **S5b**. The current and voltage output after rectification are 80  $\mu\text{A}$  and 800 V, respectively.

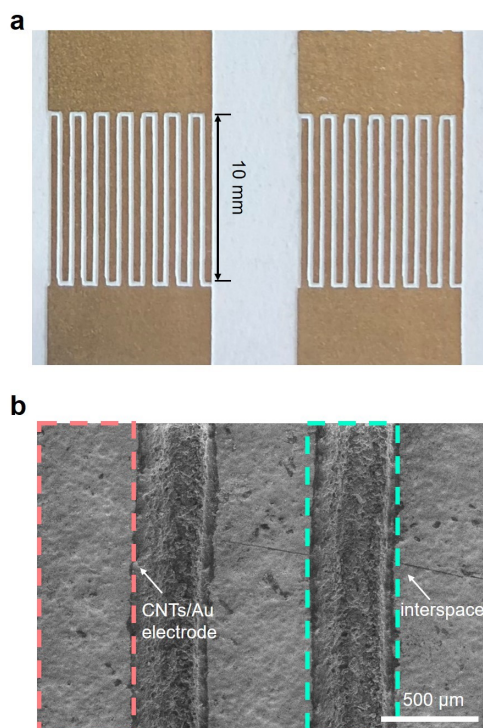
**Figure S5c** shows the durability test of the paper-TENG. The output current monitored for 10,000 s remains stable at  $\sim 85 \mu\text{A}$ .



**Supplementary Figure 5 | Rectified electrical outputs and the durability test of the paper-TENG module.** **a**, Output current and **b**, output voltage of the paper-TENG after rectification. **c**, Durability test of the paper-TENG with output current monitored for 10,000 s.

## 6. Photograph and SEM images of the MSC module with interdigitated electrodes

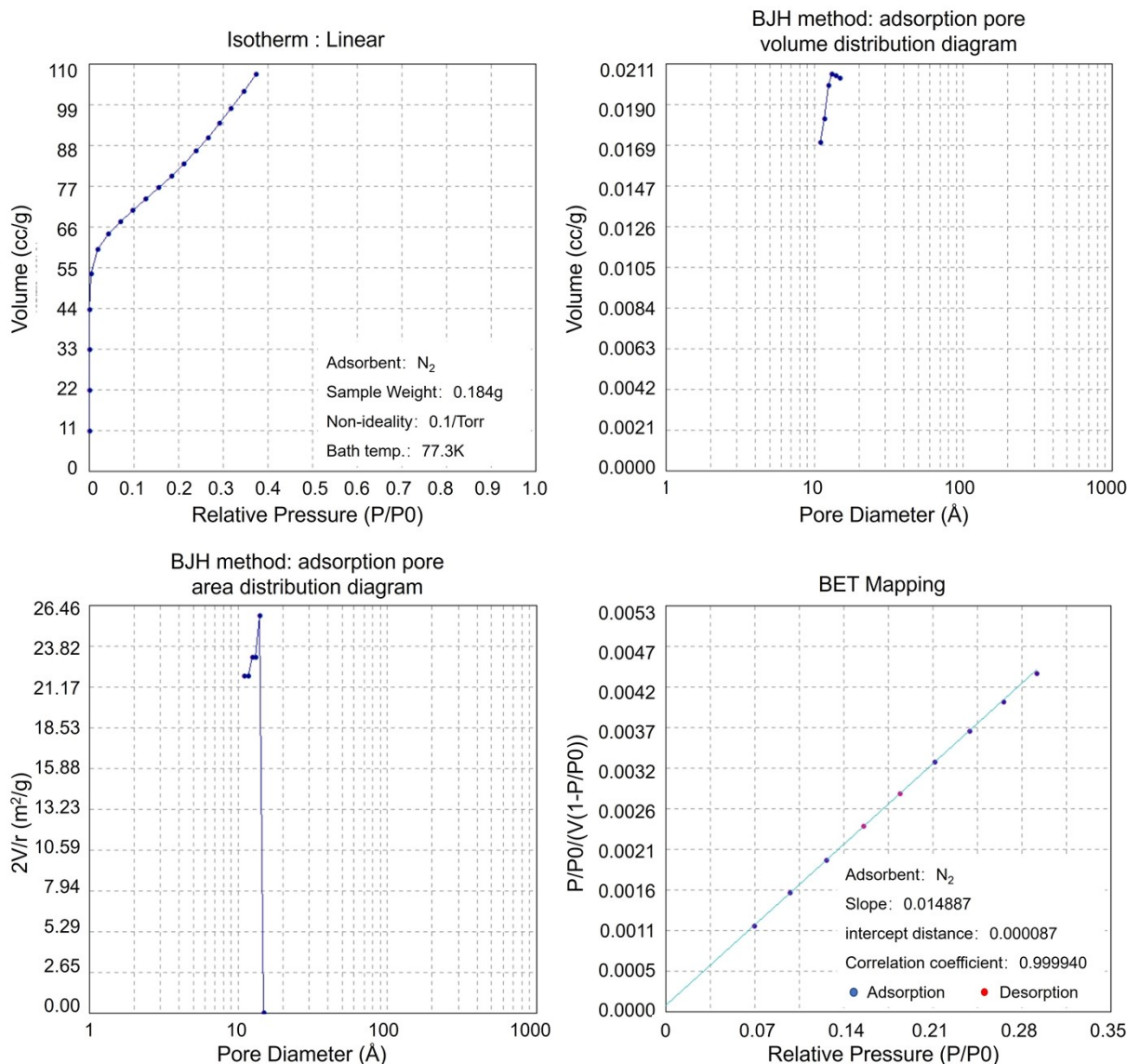
**Figure S6a** shows a photograph of the MSC module with interdigitated electrodes patterned in a length ( $L$ ) of 10 mm, a width ( $W$ ) of 0.3 mm, and an interspacing distance ( $D$ ) of 0.4 mm. Enlarged SEM images of the interdigitated electrodes are shown in **Figure S6b**. After patterning the CNT/Au film by a laser-engraving process, the interdigital CNT/Au electrodes are clearly observed with relatively flat surfaces, while the interspaced trenches (i.e., the laser-engraving traces) show a rough surface morphology with microstructures which may be induced by the inevitable residual heat during the laser-engraving process.



**Supplementary Figure 6 | Photograph and SEM image of the MSC module with interdigitated electrodes. a,** Photograph of the MSC module with interdigitated electrodes. **b,** SEM image of the interdigitated electrodes.

### **7. Brunauer–Emmett–Teller (BET) analysis of deposited CNTs**

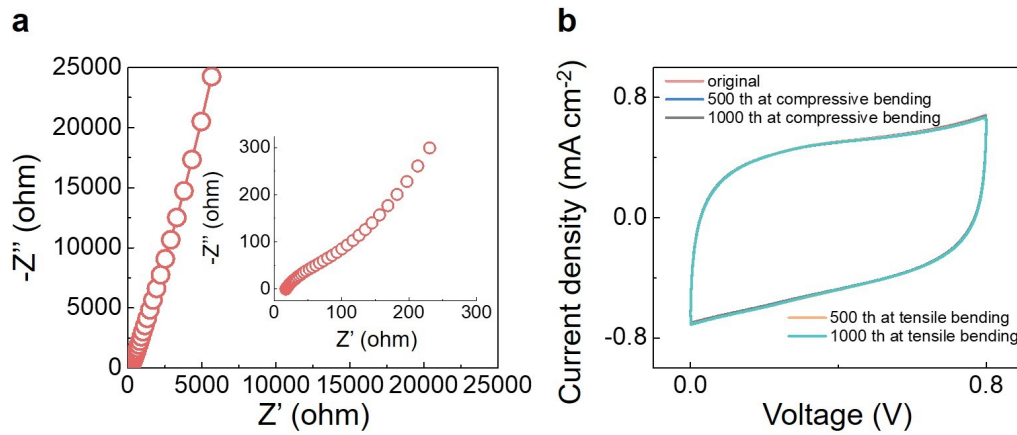
The BET test results show that the multi-point BET specific surface area is 291.149 m<sup>2</sup>/g, the total pore volume at a single point ( $r = 15.2 \text{ \AA}$ ,  $P/P_0 = 0.373830$ ) is 0.166884 cc/g, and the average pore radius at a single point (in terms of BET specific surface area) is 11.5 Å. The test equipment is SSA-6000 pore size and specific surface area analyzer.



**Supplementary Figure 7 | BET analysis of deposited CNTs.**

## 8. Nyquist plots and cyclic stability tests for the MSC module under tensile/compressive bending states

Nyquist plots of the MSCs are characterized in the frequency range from 0.01 Hz to 100 kHz. Nearly vertical straight lines are observed in the low-frequency region, which suggests excellent capacitive behavior with ultrafast ion transportation speed (**Figure S8a**). The enlarged high frequency region (inset of **Figure S8a**) indicates that the equivalent series resistance (ESR) is small at  $\sim 15 \Omega$ . The CV curves for the cyclic stability tests (at a high scan rate of  $1 \text{ V}\cdot\text{s}^{-1}$ ) under the tensile and compressive bending states are shown in **Figure S8b**. The results show that there are almost no changes in the CV curves when the MSCs are characterized for up to 1000 cycles under each bending state, which indicates that the MSC module has excellent cyclic stability and mechanical durability.



**Supplementary Figure 8 | Nyquist plots and CV curves for the MSC module under tensile/compressive bending states.** **a**, Nyquist plots of the MSC in the frequency range of 0.01 Hz to 100 kHz. The ESR extracted from the Nyquist plots is 15  $\Omega$ , which indicates good electrode conductivity, electrode-current collector contact, and electrolyte conductivity. **b**, CV curves for the cyclic stability tests of the MSC module under tensile/compressive bending states (at a high scan rate of 1  $\text{V}\cdot\text{s}^{-1}$ ).

## 9. Operation mechanism of the power management circuit (PMC) module

### a) PIN functions:

The initially rectified voltage from the TENG is input from **VIN** (or **VIN2**). A capacitor on this pin serves as an energy reservoir and input supply for the buck regulator. **CAP** is the internal rail referenced to **VIN** (or **VIN2**) to serve as gate drive for the buck PMOS (or NMOS) switch. A 1  $\mu\text{F}$  capacitor is connected between **CAP** and **VIN**. **SW** is the switch pin for the buck switching regulator. The **VOUT** is the sense pin used to monitor the output voltage and adjust it through internal feedback. A 10  $\mu\text{H}$  (or larger inductor) is connected from **SW** to **VOUT**. **D0** and **D1** are the output-voltage select bits, which can be tied high to **VIN2** or low to **GND** to select the desired **VOUT**. **VIN2** also serves as a logic high rail for output-voltage select bits **D0** and **D1**. A 4.7  $\mu\text{F}$  capacitor should be connected from **VIN2** to **GND**. The relevant position of each pin is shown in the circuit diagram of **Figure S9**.

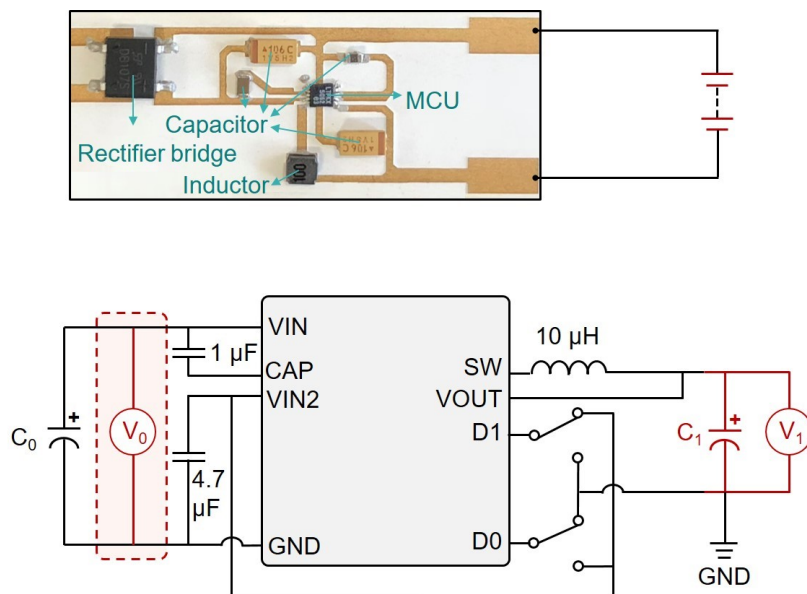
### b) Operation mechanism:

The rectified output is first stored in a capacitor on the **VIN** pin, which can be used as an energy reservoir for the buck converter. When the voltage on **VIN** rises above the undervoltage lockout (UVLO) rising threshold, the buck converter is enabled and the charges will be transferred from the input capacitor to the output capacitor.

**CAP** and **VIN2** (two internal rails) are generated from **VIN** and used to drive the high-side PMOS and low-side NMOS in the buck converter, respectively. The **VIN2** rail is regulated at

4.8 V above the GND, while the CAP rail is regulated at 4.8 V below  $V_{IN}$ . Bypass capacitors are connected to the CAP and  $V_{IN2}$  pins to serve as energy reservoirs for driving the buck switches. When  $V_{IN}$  is below 4.8 V,  $V_{IN2}$  is equal to  $V_{IN}$ , and CAP is held at GND. The  $V_{IN2}$  rail also serves as the logic high for output-voltage select bits D0 and D1 and adjust the  $V_{OUT}$ .

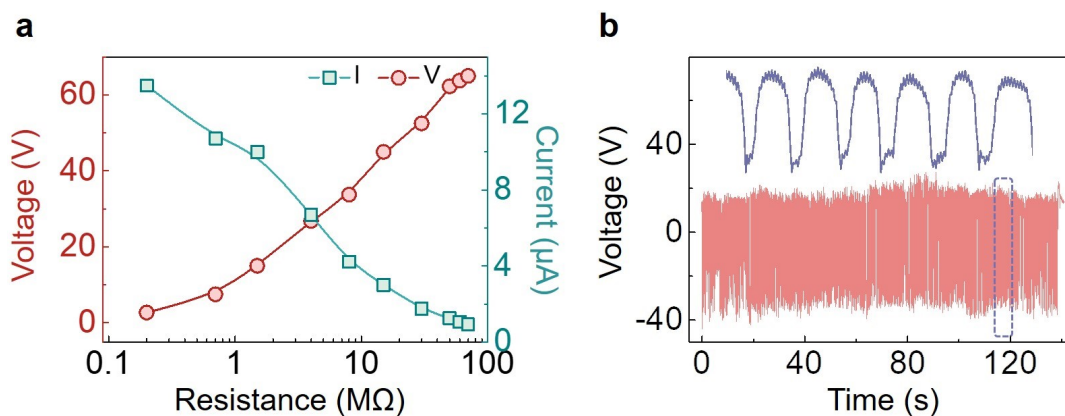
The buck regulator uses a hysteretic voltage algorithm to control the output through internal feedback (monitored from the  $V_{OUT}$  sense pin). The buck converter can charge the output capacitor to a specific value (slightly higher than the regulation point) through the inductor, which is realized by ramping the inductor current up to 260 mA through an internal PMOS switch and then ramping it down to 0 mA through an internal NMOS switch. This process efficiently delivers the harvested (rectified) energy to the output capacitor.



**Supplementary Figure 9 | Photo image and circuit diagram of power management circuits.**

### 10. The output performance of the paper-TENG under palm tapping

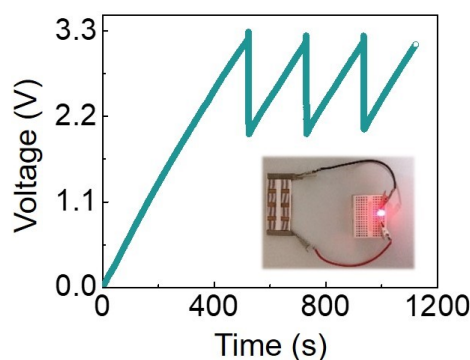
The output voltage and current of the paper-TENG under palm tapping according to different load resistances are shown in **Figure S10a**. The maximum power generated by the paper-TENG under palm tapping is calculated to be  $341.3 \mu\text{W}$  with the optimum load resistance at  $3 \text{ M}\Omega$  according to Ohm's law. The real-time output voltage of the paper-TENG under palm tapping is monitored for 140 s, as shown in **Figure S10b**. Stable output can be achieved due to the excellent robustness of the paper-TENG, which is critical as a continuous power supply to back-end applications.



**Supplementary Figure 10 | Output performance of the paper-TENG under palm tapping.** **a**, Dependence of the output voltage and current of the paper-TENG vs. different load resistances. **b**, Voltage output of the paper-TENG under palm tapping for 140 s.

### 11. Real-time charging/discharging test for the paper-based MSC

The paper-based MSC can be charged to 3.3 V within 523 s in the first charging cycle. After discharging to 1.9 V, the capacitor can be recharged to 3.3 V in 200 s with excellent charging/discharging stability (**Figure S11**). Eight MSCs in serial and parallel hybrid connections on the paper module can also be readily charged to power an LED (inset of **Figure S11**). The paper-based MSCs can be used to power the LED multiple times, representing good repeatability and stability.

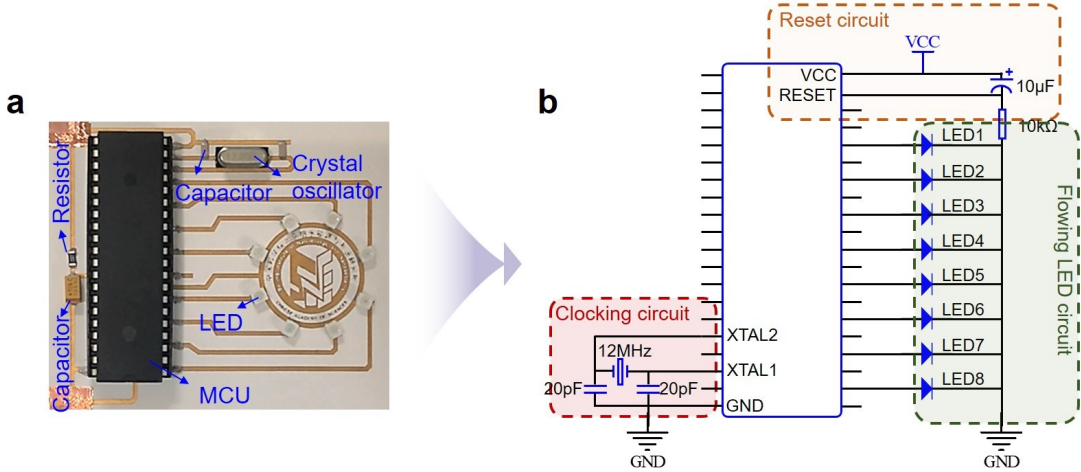


**Supplementary Figure 11 | Real-time charging/discharging test for paper-based MSCs.** Real-time charging and discharging of the paper-based MSCs. The inset is an LED driven by the paper module of serial/parallel MSCs.

### 12. Photo image and circuit diagram of the paper module for flowing LEDs

A Photo of the paper module for flowing LEDs is shown in the left panel. Its circuit diagram is shown in the right panel. The reset circuit is used to initialize the operation of the microcontroller unit (MCU). Before operating, the MCU needs to be reset first (by the reset

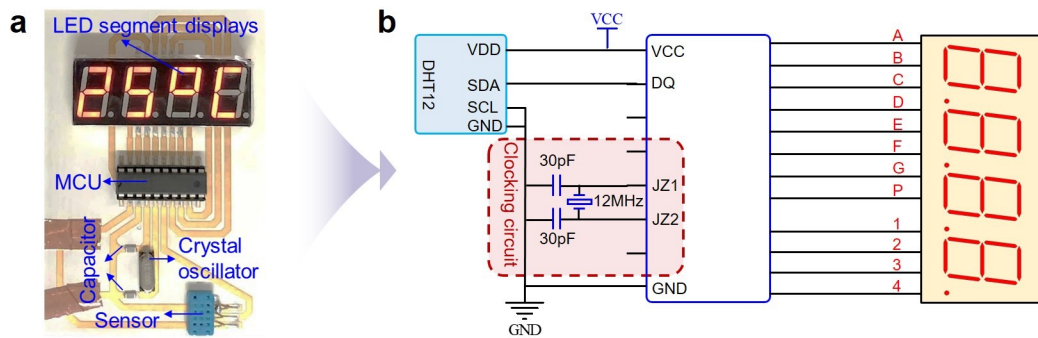
circuit) to 'return to zero'. At this moment, the MCU and other electronic components are set in a unified initial state (i.e., the start point). If one wants to light up LED1, the pin connected with LED1 is required to read a low-level signal; otherwise, LED1 will be turned off. Other LEDs are also ready to be turned on and off in the same way as LED1. Thus, the eight pins connected with LED1 ~ LED8 can be programmed to input high/low-level signals periodically with a time delay to make the LED blink and lead to the light-flowing phenomena. Notably, due to the visual delay effect of human eyes and the short execution time of each instruction by the MCU, the control diode needs to be delayed for a certain time to ensure the "flowing" effect.



**Supplementary Figure 12 | Photo image and circuit diagram of the paper module for flowing LEDs.**

**13. Photo image and circuit diagram of the paper module for the temperature/humidity sensors**

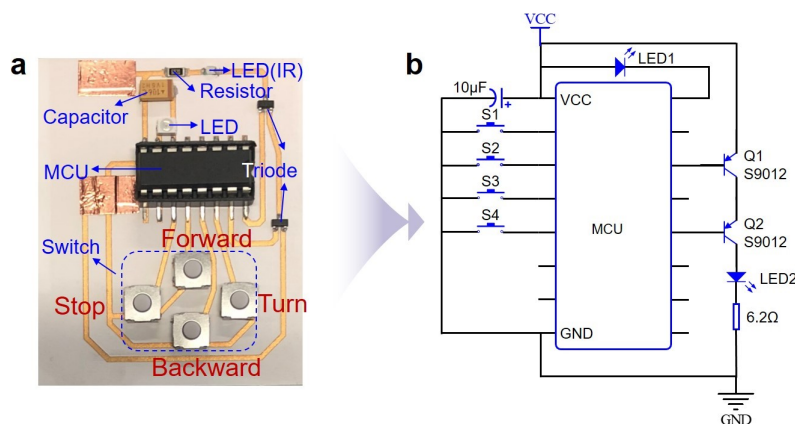
The DHT12 digital temperature/humidity sensor is a hybrid temperature and humidity sensor, that can display a calibrated digital signal output. It combines a specialized digital acquisition technique and an advanced temperature/humidity sensing mechanism to ensure high reliability and excellent long-term stability of the product. According to the circuit diagram of DHT12, the 1-wire bus communication is selected to ground the SCL pin. The role of the clock circuit with a 30 pF capacitor and 12 MHz crystal oscillator is to generate the timing signal so that the MCU will follow a certain timing rule to conduct the next instruction. The SDA pin synchronizes the sensor data with the MCU for communication and shows it on the digital segment display, thus realizing the real-time indication of surrounding temperature and humidity. Benefiting from the ultrasmall size and low power consumption of DHT12, it is suitable for integration with other electronic components for a variety of applications.



**Supplementary Figure 13 | Photo image and circuit diagram of the paper module for the temperature/humidity sensor.**

#### 14. Photo image and circuit diagram of the paper module for the IR remote controller

For the paper module of the infrared (IR) remote controller, the MCU is controlled by wireless transmitting and receiving modules. In this way, the MCU can translate and transmit corresponding instructions to realize the demanded functions. For instance, when we press the switch (S1~S4) in sequence, the remote controller can be triggered to send out a series of binary pulse codes (IR signals) with high/low level conversions according to certain timing rules. Then the remote controller can deliver corresponding information to the playmobile, conducting the action orders of moving forward/backward, stopping, and turning. To prevent undesired interference from other signals during the wireless transmission process, the IR signal is usually modulated at a specific carrier frequency (38K IR carrier signal) and transmitted via an IR transmitting diode (i.e., IR LED in the photo image). At the same time, the infrared receiver on the playmobile needs to decode the transmitted signal, which is transmitted back to the MCU through the wireless IR sensor for signal decoding and recognition. Through signal feedback, facile remote control on the playmobile is successfully realized by the functional paper module.

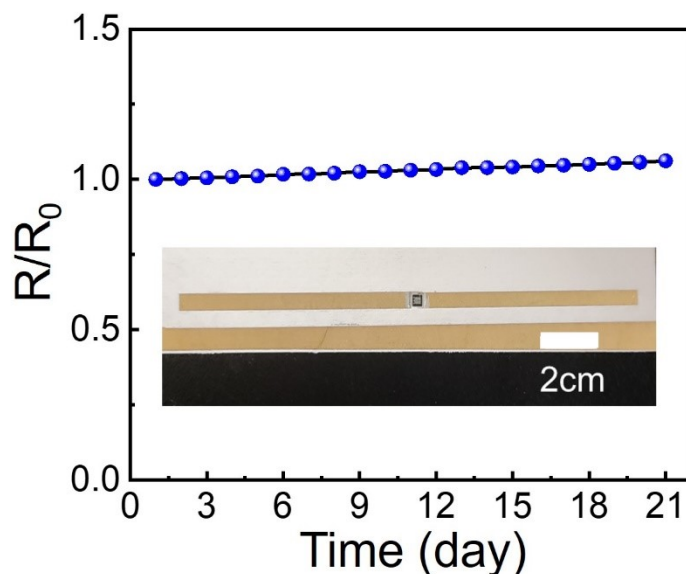


**Supplementary Figure 14 | Photo image and circuit diagram of the paper module for the IR wireless controller.**

## 15. Characterization of the sustainability of CNT/Au hybrid electrodes and functional paper modules

The functional circuits as demonstrated in **Figure 5** are mainly including the commercial electronic elements and interconnections with CNT/Au hybrid electrodes. As the commercial electronic elements are commonly reliable, the sustainability or reliability of the functional module is closely related with the resistance variation of the CNT/Au hybrid electrodes. For relevant characterizations, we first prepare CNT/Au electrode (length is 20 cm, width is 1 cm) on Teslin paper with a mounted resistor (300  $\Omega$ ). Then we have tested the change of resistance after long-term use (or standing time) for 21 days. From the test results as shown in **Figure S15**, the relative resistance variation ( $R/R_0$ , ratio of measured resistance value  $R$  to the initial resistance  $R_0$ ) is only 0.062. This increment is small and does not affect the normal operation of the functional circuits, which provides the prerequisite to the potential long-term reliability of our functional paper modules.

Furthermore, we have recorded the operating state of each functional circuit every three days by discharging/recharging the lithium-ion battery through the paper-based energy supply component. Each functional paper module can operate well as recorded in **Table S4**.



**Supplementary Figure 15 | Sustainability test for the paper-based resistive circuit (300  $\Omega$  resistor).** Relative resistance variation ( $R/R_0$ , ratio of measured resistance value  $R$  to the initial resistance  $R_0$ ) vs. Time.

**Supplementary Table 1. Comparison of the energy autonomous paper modules and commercial flexible printed circuits.**

Cons and pros		Energy autonomous paper modules	Commercial flexible circuits
<b>Materials</b>	Substrate	Teslin paper, A4 paper, white cardboard, cellulose nanopaper, etc.	Polyimide, Polyethylene terephthalate, Polyvinyl chloride, etc.
	Foldability	○	○
	Tailorability	○	×
	Biodegradability	○	×
	Electrodes	Metals, graphene, CNTs, CNT/Au, AgNWs, PEDOT:PSS, EGaIn, etc.	Metals (copper)
<b>Process</b>	Processing tech.	Laser engraving, ink-jet printing, reel-to-reel, etc.	Photolithography, wet etching
	Resolution	General (10 to 100 $\mu\text{m}$ )	High (1 to 10 $\mu\text{m}$ )
	Steps	One-step patterning, numerically-controlled direct-writing	Three-step patterning (photopatterning, developing, etching)
	Time	Fast, time-efficient	Slow, complex
	Size	Large (available > 1 m <sup>2</sup> )	Small, limited by photomask
<b>Functions</b>	Energy harvesting	○	×
	Energy storage	○	○
	Power management	○	○
	Functional circuits	○	○

From the aspect of material, paper material is one of the candidates to the substrate of commercial electronics due to its ultralow cost, biodegradability, and environmentally friendly characteristics, which may realize a truly “ubiquitous computing” network due to the facile foldability and tailorability (to prepare 3D or stretchable electrical circuits). From the manufacturing perspective, paper material is compatible with large-area reel-to-reel processing and is promising for bulk production especially when accompanied with fast and economy direct-writing methodology (e.g., laser-engraving technique, inkjet printing). Furthermore, paper substrate can be readily modified to be hydrophobic/hydrophilic or even fire-retardant on demands meanwhile retaining the biodegradable body material. Compared to the plastic substrate (e.g., PI, PET, PVC), paper is cheap, common substance (in daily life), and appropriate organic-based substrate. Specifically, Teslin paper is an eco-friendly and recyclable material,

whose main components are polyolefin and silicon oxide. When it is burned, only carbon dioxide, water, and ash (silicon oxide) are produced, which will not pollute the environment.

From the aspect of processing, commercial flexible PI circuits rely on complex photolithography and wet-etching process, which generally includes several preparation steps and multiple cycles. Additional photomask, photoresists, developer, and etchants are required, which may bring potential environment problems and additional costs. For the paper substrate, the adopted laser engraving process is a numerically-controlled direct-writing method. The pre-designed electrodes (or interconnections) are facile to be directly patterned on paper substrate without photomask and photoresist, which is time-efficient and easy for trial and error. Moreover, laser engraving can be fast processed in a few seconds or minutes depending on the circuit layouts. Regarding to the resolution, the adopted laser engraving equipment (LM-9060, Jinan Lasermen CNC Equipment Co, LTD) is facile to miniaturize the electrode size to 100  $\mu\text{m}$ . Better laser engraving machine is capable to further miniaturize the electrode size to 10~50  $\mu\text{m}$ . This resolution is lower than that achieved by the commercial flexible circuits (ideally ~1  $\mu\text{m}$ , the photolithography limitation), but it can satisfy the requirements of a certain range of applications. Besides, laser engraving technique is applicable to large-area direct-patterning (1 m  $\times$  1 m for LM-9060), which can be further enlarged with different equipment models (or custom facility).

From the aspect of functions, the proposed sustainable paper module delivers a prototype combining energy harvesting, energy storage, power management, and energy applications (functional circuits). The functional paper modules are capable of harvesting surrounding (bio)mechanical energy, converting it into DC output for efficient energy storage in MSCs or batteries, and driving the back-end functional circuits. Combining the demanded functional circuits, the incorporated paper modules can readily work in an energy-autonomous way. The proposed paper modules can also be implemented either in a discrete-unit fashion or as a customized integration module. Its working process implies an energy circulation from mechanical energy conversion into AC electricity (regulated into DC output), energy storage in electrochemical form, and energy utilization in functional circuits. The energy-autonomous paper modules and function circuits provide complementary paradigm to augment conventional flexible circuits. The advantages and disadvantages are summarized in **Table S1**.

**Supplementary Table 2. Parameters of Teslin paper.**

Model	SP 1400
Whiteness index	75
Maximum shrinkage rate (%)	4
Working temperature (°C)	-70 ~ 200
Density (g/cm <sup>3</sup> )	0.6 ~ 0.7
Modulus (N/cm)	8.5
Tear strength (g/force)	80
Ductility (%)	200

**Supplementary Table 3. Summary and comparison of some typical flexible electrodes.**

Electrode Material	Patterning Technique	Electrical conductivity(S/m)	Application	Ref
Green hydrogen bonded network	Physical Cutting	$3.6 \times 10^3$	Repairing circuits, Lighting the LEDs	1
Au/Ti	Etching	$9.6 \times 10^3$	Flexible and stretchable electronics	2
Graphene	/	50	Graphene spin circuits	3
MWCNT/MPDMS	/	1.16	Lighting the LEDs, Construct electroluminescent devices	4
Organic semiconductor composites	Multiphoton lithography	$5.4 \times 10^4$	Microresistors, Microcapacitors and $\mu$ PCBs	5
Ag	Regioselective deposition	$1.20 \times 10^7$	Flexible OFET arrays	6
EGaIn	Freestanding 3D PDMS molds	$10^4$	3D stretchable conductor	7
Silver film	Photolithographic	$10^7$	Organic field-effect transistors and circuits	8
Ag NW	phase-shifting edge lithography	$1.62 \times 10^2$	Flexible transparent nanomesh electrodes (FTNEs)	9
PEDOT:PSS	/	$3.95 \times 10^4$	Transparent electrodes	10
PPy-pTs/Au microfilms	/	13.98	Stretchable electronics, Mg battery electrodes	11
rGO/PEDOT/PSS	Laser engraving	/	Flexible microsupercapacitors	12
Laser-induced graphene	Laser engraving	/	LIG microsupercapacitors	13
CNT/Au hybrid electrode	Laser engraving	$5.70 \times 10^7$	Supercapacitor, Functional circuit modules	Our study

**Supplementary Table 4. The working sustainability of the functional paper module.**

Functional Paper Modules	Time (days)						
	1	3	6	12	15	18	21
Flowing LEDs	O	O	O	O	O	O	O
Temperature/Humidity sensor	O	O	O	O	O	O	O
IR remote controller	O	O	O	O	O	O	O

Note: "O" --- Normal working; "x" --- Not working

### Supplementary References

1. J. Hou, M. Liu, H. Zhang, Song, X. Jiang, A. Yu, L. Jiang, and B. Su, *J. Mater. Chem. A*, 2017, **5**,13138-13144.
2. G. S. Jeong, D. H. Baek, H. C. Jung, J. H. Song, J. H. Moon, S. W. Hong, I. Y. Kim, and S. H. Lee, *Nat. Commun.*, 2012, **3**, 977.
3. I. G. Serrano, J. Panda, F. Denoel, O. Vallin, D. Phuyal, O. Karis, and M. V. Kamalakar, *Nano. Lett.*, 2019, **19**,666-673.
4. X. Zhong, H. Hu, and H. Fu, *ACS Appl. Mater. Inter.*, 2018, **10**, 25697-25705.
5. O. Dadras-Toussi, M. Khorrami, A. S. C. Louis Sam Titus, S. Majd, C. Mohan, and M. R. Abidian, *Adv. Mater.*, 2022, **34**, e2200512.
6. D. Ji, L. Jiang, Y. Guo, H. Dong, J. Wang, H. Chen, Q. Meng, X. Fu, G. Tian, D. Wu, et al., *Adv. Funct. Mater.*, 2014, **24**, 3783-3789.
7. J. Park, S. Wang, M. Li, C. Ahn, J. K. Hyun, D. S. Kim, D. K. Kim, J. A. Rogers, Y. Huang, and S. Jeon, *Nat. Commun.*, 2012, **3**, 916.
8. D. Ji, L. Jiang, H. Dong, Q. Meng, Y. Zhen, and W. Hu, *J. Mater. Chem. C*, 2014, **2**, 4142.
9. S. I. Chung, P. K. Kim, T. G. Ha, and J. T. Han, *Nanotechnology*, 2019, **30**, 125301.
10. M. Vosgueritchian, D. J. Lipomi, and Z. Bao, *Adv. Funct. Mater.*, 2012, **22**, 421-428.
11. C. Wang, W. Zheng, Z. Yue, C. O. Too, and G. G. Wallace, *Adv. Mater.*, 2011, **23**, 3580-3584.
12. Y. Liu, B. Weng, Q. Xu, Y. Hou, C. Zhao, S. Beirne, K. Shu, R. Jalili, G. G. Wallace, J. M. Razal, and J. Chen, *Adv. Mater. Tech.*, 2016, **1**, 1600166.
13. J. Lin, Z. Peng, Y. Liu, F. Ruiz-Zepeda, R. Ye, E. L. Samuel, M. J. Yacaman, B. I. Yakobson, and J. M. Tour, *Nat. Commun.*, 2014, **5**, 5714.